

See discussions, stats, and author profiles for this publication at: <https://www.researchgate.net/publication/301651528>

Jin PRL2016

Dataset · April 2016

READS

32

5 authors, including:



Krishna Iyer

UPMC

21 PUBLICATIONS **93** CITATIONS

[SEE PROFILE](#)



Eric A Hoffman

University of Iowa

687 PUBLICATIONS **15,451** CITATIONS

[SEE PROFILE](#)

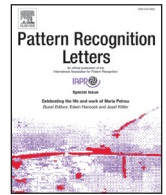


Punam K Saha

University of Iowa

219 PUBLICATIONS **5,441** CITATIONS

[SEE PROFILE](#)



A robust and efficient curve skeletonization algorithm for tree-like objects using minimum cost paths[☆]



Dakai Jin^a, Krishna S. Iyer^b, Cheng Chen^a, Eric A. Hoffman^b, Punam K. Saha^{a,b,*}

^a Department of Electrical and Computer Engineering, University of Iowa, Iowa City, IA, USA

^b Department of Radiology, University of Iowa, Iowa City, IA, USA

ARTICLE INFO

Article history:

Available online 15 April 2015

Keywords:

Curve skeletonization
Distance transform
Center of maximal ball
Minimum cost path
CT imaging
Airway tree

ABSTRACT

Conventional curve skeletonization algorithms using the principle of Blum's transform, often, produce unwanted spurious branches due to boundary irregularities, digital effects, and other artifacts. This paper presents a new robust and efficient curve skeletonization algorithm for three-dimensional (3-D) elongated fuzzy objects using a minimum cost path approach, which avoids spurious branches without requiring post-pruning. Starting from a root voxel, the method iteratively expands the skeleton by adding new branches in each iteration that connects the farthest quench voxel to the current skeleton using a minimum cost path. The path-cost function is formulated using a novel measure of local significance factor defined by the fuzzy distance transform field, which forces the path to stick to the centerline of an object. The algorithm terminates when dilated skeletal branches fill the entire object volume or the current farthest quench voxel fails to generate a meaningful skeletal branch. Accuracy of the algorithm has been evaluated using computer-generated phantoms with known skeletons. Performance of the method in terms of false and missing skeletal branches, as defined by human experts, has been examined using *in vivo* CT imaging of human intrathoracic airways. Results from both experiments have established the superiority of the new method as compared to the existing methods in terms of accuracy as well as robustness in detecting true and false skeletal branches. The new algorithm makes a significant reduction in computation complexity by enabling detection of multiple new skeletal branches in one iteration. Specifically, this algorithm reduces the number of iterations from the number of terminal tree branches to the worst case performance of tree depth. In fact, experimental results suggest that, on an average, the order of computation complexity is reduced to the logarithm of the number of terminal branches of a tree-like object.

© 2015 Elsevier B.V. All rights reserved.

1. Introduction

Skeletonization provides a simple and compact representation of an object while capturing its major topologic and geometric information [5,31,48,59]. The notion of skeletonization was initiated by Blum's pioneering work on grassfire transform [5,6] and has been applied to many image processing and computer vision applications including object description, retrieval, manipulation, matching, registration, tracking, recognition, compression etc. Following Blum's grassfire propagation the target object is assumed to be a grass-field that is simultaneously lit at its entire boundary. The fire burns the grass-field and propagates inside the object at a uniform speed and the skeleton is formed by quench points, where independent fire fronts

collide [20,28,29,33,54,58,59]. Different computational approaches for skeletonization are available in literature, some of which are widely different in terms of their principles [1,2,20,28,29,32,33,37–40,44,47,54,58,59,66]. Several researchers have used continuous approaches to compute skeletons [20,23,28,29,33,38,58] while others have used purely digital methods [32,37,39,40,44,47,54,66]. Discussion on different principles of skeletonization algorithms has been reported by Siddiqi and Pizer [59] and Saha et al. [48].

Digital skeletonization algorithms simulate Blum's grass-fire propagation using iterative erosion [31,32,37,40,47,66] or geometric analysis [1,2,4,9,43,54,66] on digital distance transform (DT) field [7,8]. In three-dimensions (3-D), a Blum's skeleton is a union of one- and two-dimensional structures, which is referred to as a *surface skeleton*. However, many 3-D objects consist only of one-dimensional (1-D) elongated structures, e.g., vascular or airway trees, for which the target skeleton is a tree of 1-D branches; such skeletons are referred to as *curve skeletons*. There are several dedicated skeletonization algorithms, called *curve skeletonization*, which directly compute curve skeletons from 3-D objects [4,21,22,56,60,62,71]. These algorithms

[☆] This paper has been recommended for acceptance by Gunilla Borgefors (3GBOR).

* Corresponding author. Tel.: +1 319 335 5959; fax: +1 319 335 6038.

E-mail address: punam-saha@uiowa.edu, pk_saha@engineering.uiowa.edu, pk_saha@healthcare.uiowa.edu (P.K. Saha).

have been broadly applied in animation [17,68], decomposition of objects [57], shape matching [10,16], colonoscopy [24,69] and bronchoscopy [30,36], stenosis detection [12,21,55,61,63,73], pulmonary imaging [25,67], micro-architectural analysis of trabecular bone [11,53] etc. This paper presents a new curve skeletonization algorithm for 3-D fuzzy digital objects using a minimum cost path approach.

Curve skeletonization approaches may be further classified into two major categories, namely, erosion based [32,39,43,40,41] and minimum cost path based approaches. Hassouna and Farag [23] presented a different framework to compute the curve skeleton of volumetric objects using level sets and gradient vector flow. The erosion-based curve skeletonization algorithms keep peeling boundary voxels, while preserving object topology and its elongated structures. Pudney [43] used DT-based erosion to directly compute the curve skeleton where only curve-end points are preserved to capture elongated structure in a 3-D object. Also, there are a few erosion- or DT-based skeletonization algorithms which compute curve skeletons in two steps [2,47] – computation of surface-skeleton from a 3-D object and then computation of curve skeleton from the surface skeleton. However, the two-steps algorithms are computation less efficient as compared to dedicated algorithms which directly computes curve skeletons from 3-D objects. A major challenge with erosion-based algorithms is the generation of spurious skeletal branches caused by irregularities in object boundaries, image noise, and other digital artifacts. Although, researchers have suggested post pruning algorithms to simplify skeletons [2,3,27,53], often times, the resulting skeletons are still left with some spurious branches. This is because these pruning decisions are primarily based on local features and the global significance of a branch is not fully assessed using local features. Recently, a few curve skeletonization algorithms [56] attempted to define global significance of skeletal branches in order to improve the performance of skeletal pruning steps. In contrast, the minimum cost path approach offers a different skeletonization approach, wherein a branch is chosen as a global optimum. Therefore, the global significance of a branch is naturally utilized to distinguish a noisy branch from a true branch improving its robustness in the presence of noisy perturbations on an object.

Peyré et al. [42] presented a thorough survey on minimum cost path methods and their applications. Minimal cost path techniques have been extensively used for centerline extraction of tubular structures in medical imaging [13,14,18,64,69,70]. These techniques involve deriving a cost metric [15] from the image in a way such that minimal paths correspond to the centerline of a tubular structure. Li and Yezzi [34] developed a novel approach to simultaneously extract centerlines as well as boundary surfaces of 3-D tubular objects, e.g., vessels in MR angiography or CT images of coronary arteries, using a minimal path detection algorithm in 4-D, where the fourth dimension represents the local vessel diameter. Wong and Chung [72] presented another algorithm where they, first, traced the vessel axis on a probabilistic map from a gray-scale 3-D angiogram and, subsequently, delineated the vessel boundary as a minimum cost path on a weighted and directed acyclic graph derived from cross-sectional images along the vessel axis. However, such methods connects specified end points to a source point but are not designed for computation of 3-D curve skeletons. Bitter et al. [4] presented an algorithm to compute a complete curve skeleton of a 3-D object using the minimum cost path approach. However, there are several major drawbacks and limitations of their method, which restrict the use of minimum cost path as a popular curve skeletonization approach. These drawbacks and limitations of the previous method together with their solutions are discussed in the following.

In this paper, a comprehensive and practical solution is presented for direct computation of curve skeletons from 3-D fuzzy digital objects using a minimum cost path approach. Central challenges for curve skeletonization using a minimum cost path approach

are – (1) assurance of medialness for individual skeletal branches, (2) assessment of branch significance to distinguish a true branch from a noisy one and to determine the termination condition, and (3) computational efficiency. Beside that the new algorithm is generalized for fuzzy objects, it makes major contributions to overcome each of these challenges. To assure medialness of skeletal branches, Bitter et al. [4] suggested a penalized distance function that uses several ad-hoc and scale-sensitive parameters. However, as demonstrated in this paper, their method inevitably fails to stick to the medial axis, especially at sharp turns or large-scale regions. Also, their parameters are scale-sensitive, which need to be tuned for individual objects depending on their scales. These limitations of their cost function are further exaggerated for objects containing multi-scale structures, e.g., airway or vascular trees. To solve this problem, we introduce the application of centers of maximal balls (CMBs) [54] to define path-cost that is local scale-adaptive and avoids use of parameters. It can be shown that, for a compact object in R^3 , a minimum cost path using the new approach always sticks to the Blum's skeleton. Moreover, in the previous approach a skeletal branch is extended up to an object boundary which contradicts Blum's principle at a rounded surface whereby the branch of a Blum's skeleton ends to a CMB prior to reaching an object boundary. The new method overcomes this difficulty by selecting the farthest CMB instead of object boundary points while adding a new skeletal branch. In regards to the second challenge, a local scale component is introduced while deciding the next most-significant skeletal branch, which makes a major improvement in discriminating among spurious and true branches. Finally, to reduce computational demand, a new algorithm is presented that allows simultaneous addition of multiple independent skeletal branches reducing the computational complexity from the order of the number of terminal branches to the worst-case performance of the order of tree-depth.

2. Methods and algorithms

Basic principle of the overall method is described in Section 2.1. Three major steps in the algorithm, namely, skeletal branch detection, object volume marking, and termination criterion, are described in Sections 2.2, 2.3, and 2.4, respectively. Improvements in computation performance using the new algorithm is discussed in Section 2.5. A preliminary version of our work was presented in a conference paper [26].

2.1. Basic principle

Conventional curve skeletonization algorithms are designed on the principle of Blum's grassfire transform implemented using voxel erosions, which is subjected to constraints for preservation of object topology and local "elongatedness". Generally, voxel erosion is controlled by local properties, limiting the use of larger contextual information while selecting the end point of a skeletal branch during the erosion process. Therefore, such methods often suffer from an intrinsic challenge while handling noisy structures or boundary irregularities, e.g., the small protrusion, denoted as p_{noise} in Fig. 1. The new method works for 2-D or 3-D tree-like objects (e.g., vascular or airway trees), which are simply-connected without tunnels or cavities [45,46]. The method starts with a root voxel, say o , as the initial seed skeleton, which is iteratively grown by finding the farthest CMB and then connecting it to the current skeleton with a new branch. The iterative expansion of the skeleton continues until no new meaningful branch can be found. During the first iteration, the method finds the farthest CMB p_1 from the current skeleton o . Next, the skeleton is expanded by adding a new skeletal branch joining p_1 to the current skeleton. This step is solved by finding a minimum cost path from o to p_1 (see Fig. 1a). Here, it is important that the cost function should be chosen such that the minimum cost path runs along the centerline of the object and a high cost is applied when it attempts to deviate from

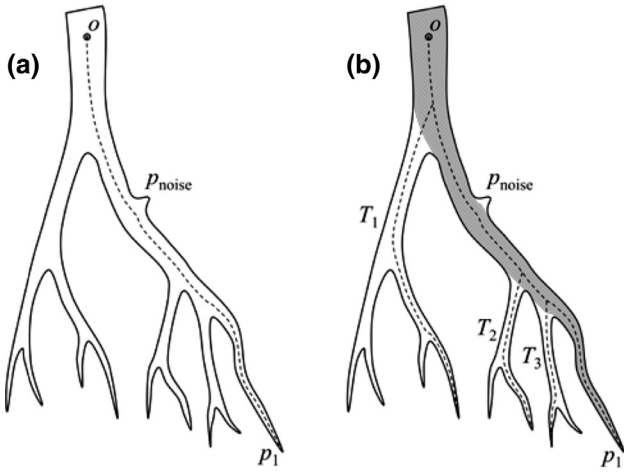


Fig. 1. Schematic illustration of the new curve skeletonization algorithm. (a) The algorithm starts with the root point o as the initial skeleton and finds the farthest CMB p_1 . Next, p_1 is connected to the skeleton with the branch op_1 computed as a minimum cost path. (b) The object volume corresponding to the current skeleton is marked (gray region) and the three skeletal branches are added where each branch connects the farthest CMB in one of the three sub-trees T_1 , T_2 , and T_3 in the unmarked object region. Note that the noisy protrusion p_{noise} does not create any noisy branch even after all meaningful branches are added to the skeleton.

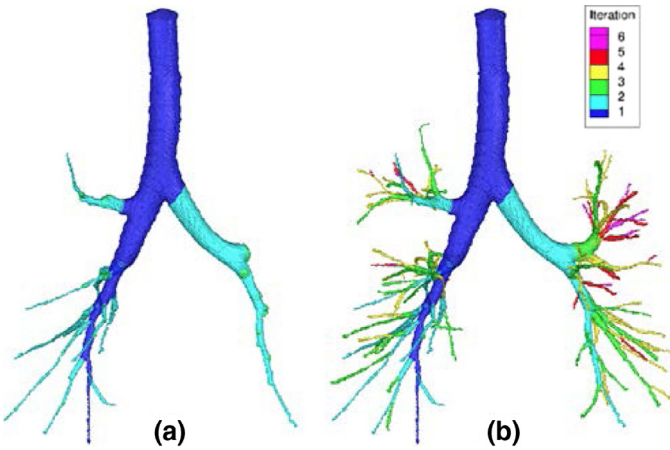


Fig. 2. Results at different iteration of the new curve skeletonization algorithm. (a) The marked object volume on a CT-derived human intrathoracic airway tree corresponding to the skeletal branches computed after two iterations. (b) Same as (a) but at the terminal iteration. (For interpretation of the references to color in this figure legend, the reader is referred to the web version of this article.)

the centerline. After the skeletal branch op_1 is found, the representative object volume is filled using a local scale-adaptive dilation along the new branch and marked as shown in Fig. 1b. In the next iteration, three skeletal branches are added where each branch connects the farthest CMB in one of the three sub-trees T_1 , T_2 , and T_3 in the unmarked region. Then the marked object volume is augmented using dilation along the three new skeletal branches. This process continues until no new meaningful branch can be found. Fig. 2 presents a color-coded illustration of the marked object volume corresponding to the branches located at different iterations.

An important feature of the new method is that the meaningfulness of an individual skeletal branch is determined by its global context. Therefore, the method is superior in stopping noisy branches. Also, the minimum cost path approach improves the smoothness of skeletal branches. Finally, depending upon the application, the initial root point may be automatically detected, e.g., (1) the point with the largest distance transform value, (2) the deepest points on topmost

plane in the airway tree etc. Major steps of the algorithm are outlined in the following.

Begin algorithm: compute-curve-skeleton

Input: the original object volume O

Output: curve skeleton S

Initialize a root voxel o as the current skeleton S and the current marked object volume O_{marked}

While new branches are found

Detect disconnected sub-trees T_1, T_2, T_3, \dots in the unmarked object volume $O - O_{marked}$

For each sub-tree T_i

Find the CMB voxel $v_i \in T_i$ that is farthest from O_{marked}

If the potential branch from v_i to O_{marked} is significant

Add a new skeletal branch B_i joining v_i to the current skeleton S using a minimum cost path

Augment $S = S \cup B_i$

Compute local scale-adaptive dilatation D_i along B_i

Augment $O_{marked} = O_{marked} \cup D_i$

End algorithm: compute-curve-skeleton

In this paper, Z^3 is used to denote a *cubic grid* where Z is the set of integers. An element $p \in Z^3$ of the grid is referred to as a *voxel*. A *fuzzy digital object* $\mathcal{O} = \{(p, \mu_{\mathcal{O}}(p)) | p \in Z^3\}$ is a fuzzy subset of Z^3 , where $\mu_{\mathcal{O}} : Z^3 \rightarrow [0, 1]$ is the *membership function*. The *support* O of \mathcal{O} is the set of voxels with non-zero membership values, i.e., $O = \{p | p \in Z^3 \wedge \mu_{\mathcal{O}}(p) \neq 0\}$. A voxel inside the support is referred to as an *object voxel*. Let $FDT_{\mathcal{O}}(p)$, where $p \in O$, denote the fuzzy distance transform [52] at an object voxel p .

Sanniti di Baja [54], introduced the seminal notion of center of maximal ball (CMB) and counselled their use as quench voxels in a binary image. Here, we use fuzzy centers of maximal balls (fCMBs) as *quench voxels* in a fuzzy digital object. An object voxel $p \in O$ is a *fuzzy center of maximal ball* (fCMB) in \mathcal{O} if the following inequality holds for every 26-neighbor q of p

$$FDT(q) - FDT(p) < \frac{1}{2} (\mu_{\mathcal{O}}(p) + \mu_{\mathcal{O}}(q)) |p - q|. \quad (1)$$

Saha and Wehrli [50], introduced the above definition of fCMB which was further studied by Svensson [65]. Also, it may be noted that the definition of fCMB is equivalent to the CMB [54] for binary digital objects.

For fuzzy objects, quench voxels are sensitive to noise generating a highly redundant set. Therefore, it is imperative to use a *local significance factor* (LSF) [27], a measure of collision impact by independent fire-fronts, to distinguish among strong and weak quench voxels. LSF of an object voxel $p \in O$ in a fuzzy digital object \mathcal{O} is defined as:

$$LSF(p) = 1 - f_+ \left(\max_{q \in N^*(p)} \frac{FDT(q) - FDT(p)}{1/2 (\mu_{\mathcal{O}}(p) + \mu_{\mathcal{O}}(q)) |p - q|} \right), \quad (2)$$

where $f_+(x)$ returns the value of x if $x > 0$ and zero otherwise; and $N^*(p)$ is the excluded 26-neighborhood of p . It can be shown that LSF at a quench voxel lies in the interval of $(0, 1]$ and it takes the value of '0' value at non-quench voxels. A quench voxel with LSF value greater than 0.5 will be called a *strong quench voxel*.

2.2. Skeletal branch detection

During an iteration of the new algorithm, multiple meaningful skeletal branches are added to the current skeleton where each branch comes from a connected sub-tree T_i in the unmarked object volume $O - O_{marked}$. Let $C_{\mathcal{O}} \subset O$ be the set of all strong quench voxels in the fuzzy digital object \mathcal{O} . To locate the branch-end voxel in each sub-tree T_i , the geodesic distance (GD) from O_{marked} is computed for each voxel in $C_{\mathcal{O}} \cap T_i$. A *path* $\pi = \langle p_0, p_1, \dots, p_{l-1} \rangle$ is an ordered sequence of voxels where every two successive voxels $p_{i-1}, p_i \in Z^3$ $i =$

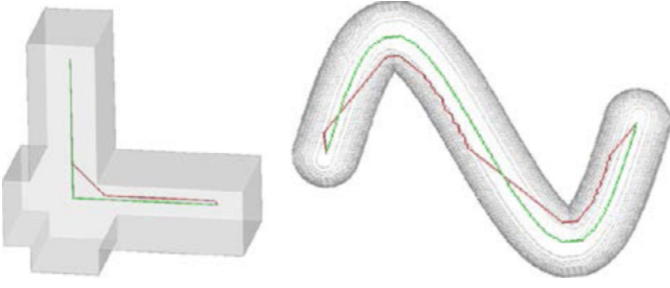


Fig. 3. Illustration of geodesics using the new path-cost function. In the left figure, the new geodesic (green) preserves the sharp corner of the shape while the path (red) by Bitter et al. fails. In the right example, the new geodesic smoothly follows the centerline of the object while Bitter et al.'s path makes several corner cutting. (For interpretation of the references to color in this figure legend, the reader is referred to the web version of this article.)

$1, \dots, l-1$, are 26-adjacent. The *length* of a path π is defined as

$$\text{length}(\pi) = \sum_{i=1}^{l-1} |p_{i-1} - p_i|. \quad (3)$$

The *geodesic distance* or *GD* of a voxel $p \in C_O \cap T_i$ from O_{marked} is computed as:

$$GD(p) = \min_{\pi \in \Pi_p} \text{length}(\pi), \quad (4)$$

where Π_p is the set of all geodesic paths from p to O_{marked} confined to O . The *branch-end voxel* in T_i is selected as farthest (in the geodesic sense) strong quench voxel v_i as follows:

$$v_i = \arg \max_{p \in C_O \cap T_i} GD(p). \quad (5)$$

It may be noted that, unlike the algorithm by Bitter et al. [4], the above equation ensures that a skeletal branch ends to quench voxel and thus agrees with the Blum's principle of skeletonization.

To ensure medialness of the skeletal branch, a minimum path-cost condition is imposed and the LSF measure is used to define the path-cost. First, the *step-cost* between two 26-adjacent voxels $p, q \in Z^3$ is defined as:

$$SC(p, q) = \frac{|p - q|}{\epsilon + (\text{average}(LSF(p) + LSF(q)))^2}, \quad (6)$$

where the parameter ϵ is a small number used to overcome numerical computational difficulties. In this paper, a constant value of '0.01' is used for ϵ . The cost $Cost(\pi)$ of a path $\pi = \langle p_0, p_1, \dots, p_{l-1} \rangle$ is computed by adding individual step-cost along the path, i.e.,

$$Cost(\pi) = \sum_{i=1}^{l-1} SC(p_{i-1}, p_i). \quad (7)$$

It can be shown that the new path cost function ensures that the minimum cost path between two skeletal points lies on Blum's skeleton; see the minimum cost path (green) between two points in each of the two shapes in Fig. 3. It is encouraging to note how the new geodesic preserves the sharp corner in the first shape while the minimum cost path function by Bitter et al. fails. In the second shape, the corner cutting by Bitter et al.'s path is obvious while the new geodesic shows a smooth traversal along the centerline of the object. The final task is to connect the selected quench voxel v_i to the current skeleton S using the minimum cost path. In other words, the path B_i connecting v_i to S is computed as:

$$B_i = \arg \min_{\pi \in \Pi_{v_i, S}} Cost(\pi), \quad (8)$$

where $\Pi_{v_i, S}$ is the set of all paths between v_i and S confined to O .

2.3. Object volume marking

The final step during an iteration is to mark the object volume represented by a newly added skeletal branch. After finding the minimum cost path, local volume marking is applied along the new skeletal branch B_i . Specifically, a local scale-adaptive dilation is applied to mark the object region along B_i . The local dilation scale $scale(p)$ at a given voxel p on B_i is defined as twice its FDT value. Efficient computation of local scale-adaptive dilation is achieved along the principle of the following algorithm.

Begin algorithm: compute-local-scale-adaptive-dilation

Input: support O of a fuzzy object

A skeletal branch B_i

Local dilation scale map $scale : B_i \rightarrow R^+$

Output: Dilated object volume O_{B_i}

$\forall p \in B_i$, **initialize** the local dilation scale $DS(p) = scale(p)$

$\forall p \in O - B_i$, **initialize** dilation scale $DS(p) = -max$

While the dilation scale map DS is changed

$\forall p \in O - B_i$, **set** $DS(p) = \max_{q \in N^+(p)} DS(q) - |p - q|$

Set the output $O_{B_i} = \{p | p \in O \wedge DS(p) \geq 0\}$

Augment the marked object volume $O_{\text{marked}} = O_{\text{marked}} \cup O_{B_i}$

End algorithm: compute-local-scale-adaptive-dilation

2.4. Termination criterion

As described earlier, the algorithm iteratively adds skeletal branches and it terminates when no more significant skeletal branch can be found. Specifically, the termination is caused by two different situations – (1) the marked volume O_{marked} covers the entire object, or (2) none of the strong quench voxel in the unmarked region $O - O_{\text{marked}}$ generates a significant branch. The first criterion characterizes the situation when the entire object is represented with skeleton branches and no further branch is needed. The second situation occurs when there are small protrusions left in the unmarked region, however, none of those protrusions warrants a meaningful skeletal branch.

The *significance* of a branch B_i joining an end voxel $v_i \in C_O \cap T_i$ to the skeleton S is computed by adding LSF values along the path inside the unmarked region, i.e.,

$$\text{significance}(B_i) = \sum_{p \in B_i - O_{\text{marked}}} LSF(p). \quad (9)$$

A local scale-adaptive significance threshold is used to select a skeletal branch. Let $p_v \in S$ be the voxel where the branch B_i joining an strong quench voxel v meets the current skeleton S . The scale-adaptive significance threshold for the selection of the new branch B_i is set as $3 + 0.5 \times FDT(p_v)$.

Three important features of the above termination criterion need to be highlighted. First, the significance of a new branch is computed from the current marked object volume instead of the current skeleton. Second, a measure of branch significance is used instead of simple path-length, which elegantly subtracts the portion of a path merely contributing to topological connectivity with little or no significance to object shape. Finally, the new termination criterion uses a scale adaptive threshold for significance. At large-scale object regions, it is possible to visualize a situation where a branch is long enough while failing to become significant under the new criterion. Under such a situation, a large portion of the target branch falls inside the marked object volume resulting in a low significance measure. A scale-adaptive threshold of significance further ensures that such false branch at large scale regions are arrested. Final results of skeletonization for a CT-based human intrathoracic airway tree are shown in Fig. 4b. As it appears visually, the algorithm successfully traces all true branches without creating any false branches as compared to the results using Bitter et al.'s method (Fig. 4a) which creates several false branches while missing quite a few obvious ones (marked with red circles).

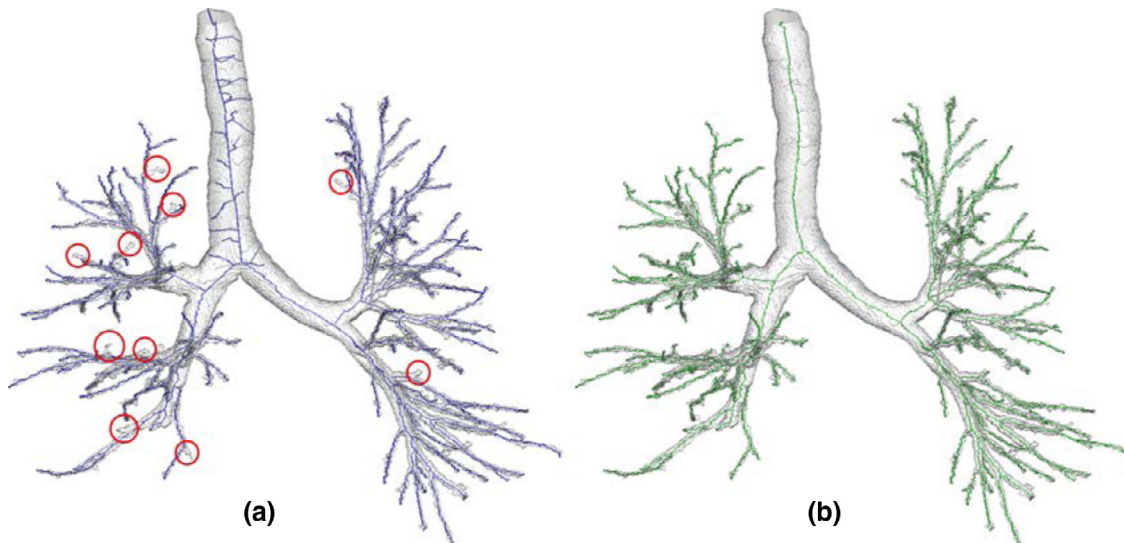


Fig. 4. Comparison of skeletal branch performance between Bitter et al.'s algorithm (a) and the new one (b) on a CT-derived human airway tree. The missing branches are marked with red circles. (a) Bitter et al.'s algorithm generates several noisy skeletal branches while already missing quite a few true branches. (b) Our method neither generates a noisy branch nor misses a visually obvious branch. (For interpretation of the references to color in this figure legend, the reader is referred to the web version of this article.)

2.5. Computational complexity

The computational bottleneck of the minimum cost path approach of skeletonization is that it requires re-computation of path-cost map over the entire object volume after each iteration. In previous methods [4,26], only one branch is added in each iteration. Therefore, the computational complexity is determined by the number of terminal branches N in the skeleton. The new algorithm makes a major improvement in computational complexity. As illustrated in Fig. 1, after adding the skeletal branch op_1 and finding the marked object volume along op_1 , the unmarked volume generates three disconnected sub-trees T_1 , T_2 , and T_3 (Fig. 1b). These three sub-trees represent the object volume for which skeletal branches are yet to be detected.

An important observation is that, since these sub-trees are disconnected, their representative skeletal branches are independent. Therefore, new skeletal branches can be simultaneously computed in T_1 , T_2 , and T_3 . In other words, in the next iteration, three branches can be simultaneously added where each branch connects to the farthest CMB within each sub-tree. After adding the three branches, the marked volume is augmented using local scale-adaptive dilation along the three new branches. This process continues until dilated skeletal branches mark the entire object volume or all meaningful branches are found. For the example of Fig. 1, algorithm terminates in four iterations while it has nine terminal branches.

This simple yet powerful observation reduces the computational complexity of the algorithm from the order of number of terminal branches to worst case performance of the order of tree-depth. For a tree with N nodes, the average depth of unbalanced bifurcating tree is $O(\sqrt{N})$ [19]. Thus, our average computation complexity is better than $O(\sqrt{N})$ as compared to $O(N)$ using previous algorithms. For a complete bifurcating tree, the number of iteration by our method is $O(\log N)$. For example, the airway tree in Fig. 2 contains 118 terminal branches and the new algorithm adds twelve skeletal branches after two iterations (Fig. 2a) and completes the skeletonization process in only 6 iterations (Fig. 2b). See Section 3.4 for more experimental results demonstrating the improvement of computational efficiency of the new method.

3. Experimental results

Figs. 2–5 qualitatively illustrate the performance of the new method. For example, Fig. 2 illustrates the improvement by the

method in terms of computation complexity where the skeleton of a tree-like object with a large number of branches is completed in a few iterations. Fig. 3 shows the superiority of the new cost function as compared to the one by Bitter et al. in tracing the center line of the target object. Fig. 4 qualitatively demonstrates the performance of the new method in handling true and noisy branches as compared to Bitter et al.'s algorithm using minimum cost path. Fig. 5 shows the robustness of the new algorithm on a variety of shapes available online, many with complex 3-D geometry. For all these figures, the method generates a skeletal branch for each visible feature while arresting noisy branches.

In the rest of this section, we present quantitative results of three experiments evaluating the method's performance in terms of accuracy, false branch detection, and computational efficiency as compared to two leading methods [32,41]. The method by Palágyi et al. was selected because it was designed for tubular tree objects and an optimized implementation for airways was obtained from the authors. The recommended value of '1' was used for the threshold parameter 't' as mentioned in [41]. Another highly cited method by Lee et al. [32], available through ITK: The NLM Insight Segmentation and Registration Toolkit, <http://www.itk.org> was used for comparison. The second method represents a decision-tree based approach for curve skeletonization. The branch performance and computation efficiency of the new method was also compared with Bitter et al.'s method.

3.1. Data and phantom generation

The performance of the method was examined on tubular tree phantoms generated from human airway and coronary artery CT images. CT images of human airway and coronary artery were used for quantitative experiments. *In vivo* human airway CT images were acquired from a previous study, whereby subjects were scanned at a fixed lung volume (total lung capacity: TLC) using a volume-controlled breath-hold maneuver. Airway images were acquired on a Siemens sensation 64 multi-row detector CT scanner using the following parameters: 120 kV, 100 effective mAs, pitch factor: 1.0, nominal collimation: 64×0.6 mm, image matrix: 512×512 , 0.55×0.55 mm in-plane resolution, and 0.6 mm slice thickness.

Airway phantom images with known skeletons were generated from five CT images as described below. The following steps were applied on each CT image – (1) segmentation of human airway lumen

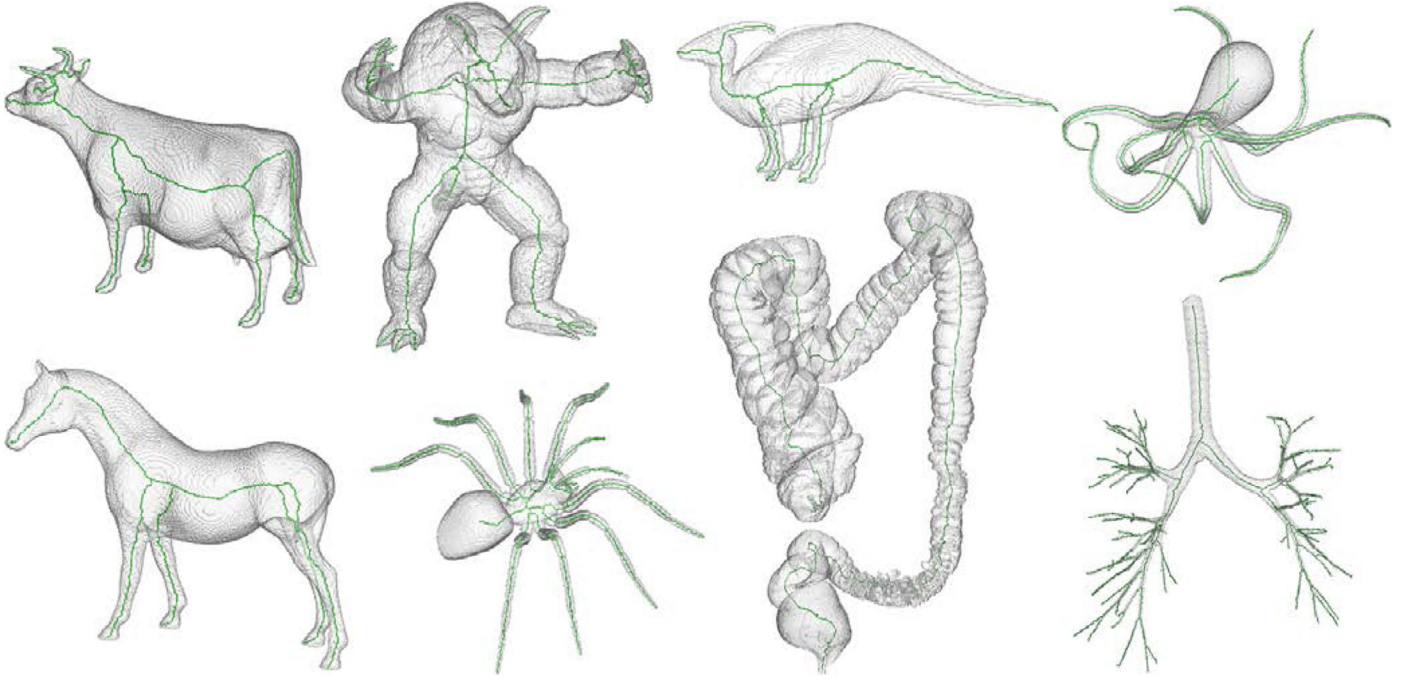


Fig. 5. Results of application of the new curve skeletonization algorithm on different 3-D volume objects available online. The object volume is displayed using partial transparency and computed skeletons are shown in green. As observed from these results, the new method does not generate any noisy branch while producing branches for all major geometric features in these objects.

from using a region growing algorithm [49], (2) curve skeletonization [47] and computation of airway lumen local thickness [35], (3) pruning of curve skeleton beyond the 5th anatomic level of branching, (4) up-sampling of the curve skeleton and local thickness map by $2 \times 2 \times 2$ voxels, (5) fitting of a B-spline to each individual skeletal branch, (6) smoothing of the thickness values along each skeletal branch, (7) reconstruction of a fuzzy object for the airway tree using local thickness-adaptive dilation along skeletal branches at $5 \times 5 \times 5$ sub-voxel resolution, (8) addition of granular noisy protrusions and dents on the airway tree boundary, (9) down-sampling of each airway tree object and its skeleton at $3 \times 3 \times 3$ voxels, and (10) filling of any small cavities or tunnels [45] artificially created while adding noisy protrusions and dents or down-sampling. For the step of adding noisy protrusions and dents, 1% of the airway boundary voxels are randomly selected as locations for protrusions or dents. The granular protrusion or dent were generated using local-scale adaptive blobs whose radius was randomly chosen from three different ranges depending upon the noise level. Specifically, $30 \pm 10\%$, $50 \pm 10\%$, and $70 \pm 10\%$ of the local scale were used for the three levels of noise. See Fig. 6 for the airway tree phantoms at different levels of noise.

Also, eight online (<http://coronary.bigr.nl/>) coronary artery datasets with known centerlines from the Rotterdam coronary centerline evaluation project [55] were used. Steps 7–10 were applied to each coronary dataset to produce four test phantom images at four different noise levels. Besides these phantom data sets ten original human airway tree data sets derived from in vivo CT imaging were used for evaluating the performance of different algorithms in terms of true/false branch and computational efficiency. Finally, the new algorithm was directly applied on these fuzzy objects while a threshold of 0.5 and filling of small cavities and tunnels were applied prior to using other methods which are essentially designed for binary objects.

3.2. Accuracy

Twenty airway (5 images \times 4 noise levels) and thirty two coronary artery (8 images \times 4 noise levels) phantoms at different levels of noise

were used to examine the accuracy of different methods. Results of application of curve skeletonization by different methods on an airway phantom data at different levels of noise are shown in Fig. 6. To quantitatively assess the performance of different methods, an error was defined to measure the difference between true and computed skeletons. As mentioned in Section 3.1, each branch in the true skeleton was represented using a B-spline. The true skeleton was expressed as a set of densely sampled points of the true skeletal branches; let S_T denote the set of N_T number of sample points on a true skeleton. Let S_C denote the set of N_C number voxels in the computed skeleton by a given method. Skeletonization error was computed as follows:

$$\text{error} = \frac{1}{2N_T} \sum_{p \in S_T} \min_{q \in S_C} |p - q| + \frac{1}{2N_C} \sum_{p \in S_C} \min_{q \in S_T} |p - q|.$$

Mean and standard deviation of errors by three skeletonization algorithms (Lee et al., Palágyi et al. and the new method) for airway and coronary phantom images are presented in Fig. 7. For both airway and coronary phantoms, the average error and standard deviation using our algorithm are less than those by Lee et al. and Palágyi et al. at all noise levels and a paired t-test confirmed that these differences are statistically significant ($p < 0.001$). Also, it is observed from the figure that the average error plus its standard deviation using our method is less than one voxel even at the highest noise level for both airway and coronary phantoms. As discussed by Saha and Wehrli [51], the average digitization error in a skeleton is close to 0.38 voxel. Therefore, after deducting the digitization error, the performance of the new method is promising.

In general, observed mean skeleton errors for coronary phantoms were higher than airway phantoms. A possible reason behind this observation is that the average thickness of coronary phantoms was greater than airway phantoms in voxel unit. At the noise free level, neither the algorithm by Lee et al. nor by Palágyi et al. produced visible false branches (see Table 1), however, the skeleton errors were significantly larger than the new method. A possible explanation behind this observed difference at noise free level is that the skeleton produced by the new method is spatially closer to the original centerline as compared to the other two methods.

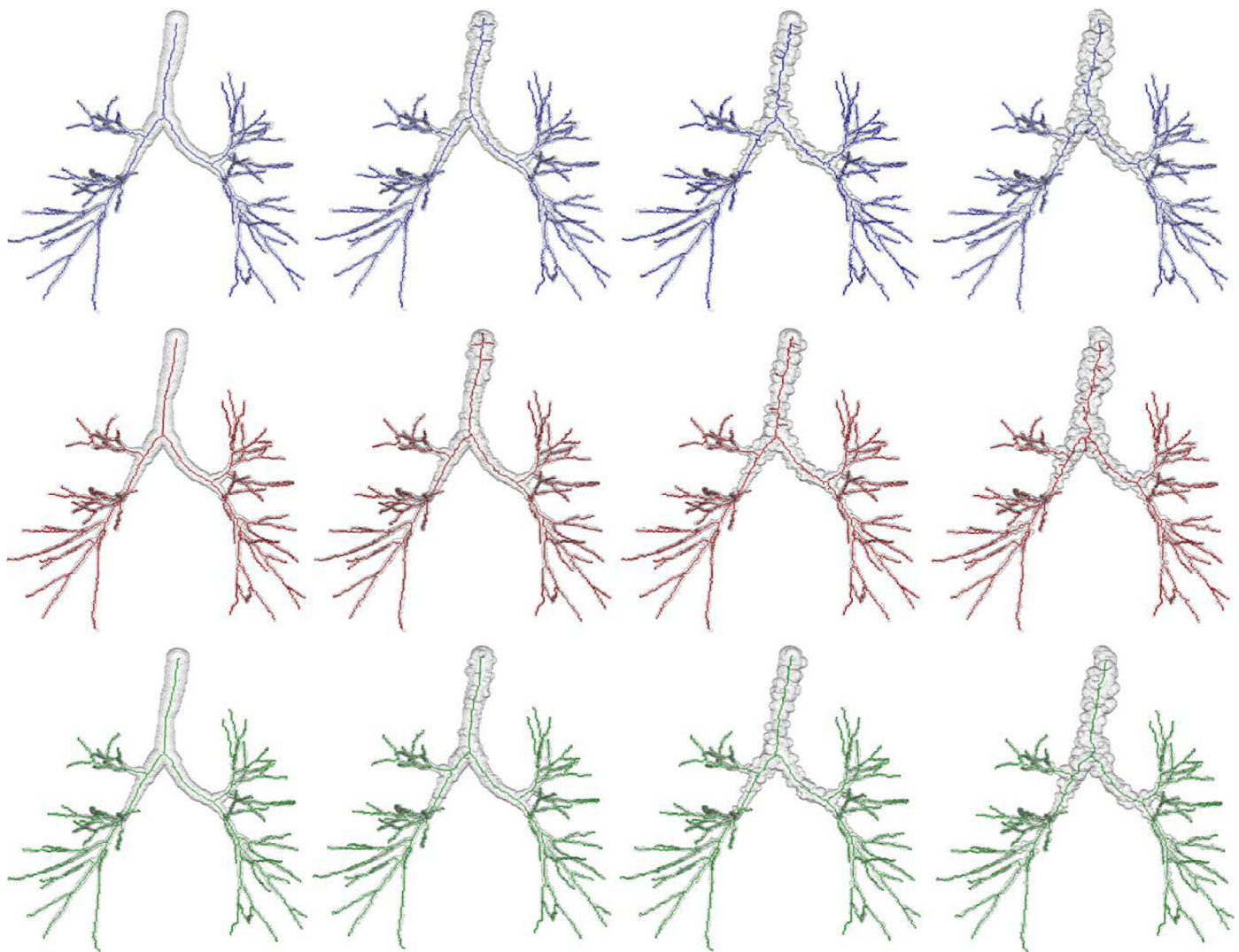


Fig. 6. Curve skeletonization results by different methods on airway phantom images at different levels of noise and down-sampling. Columns from left to right represent phantom images at no noise and low, medium, and high levels of noise. Top, middle, and bottom rows present curve skeletonization results using the methods by Lee et al., Palágyi et al. and the new method, respectively. It is observed from these figures that both Lee et al. and Palágyi et al.'s method produce several false branches at low, medium and high noise levels, while the new method produces no visible false branch. All methods have captured all meaningful branches.

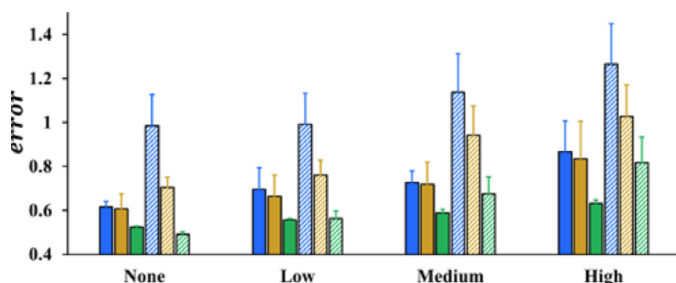


Fig. 7. Skeletonization errors by different methods on computerized phantoms at different noise levels – none, low, medium, and high. Blue, gold, and green bars represent skeleton errors by three different methods – Lee et al., Palágyi et al., and the new method. The solid bars represent the errors for airway phantoms while the bars with the slanted pattern show the errors for coronary phantoms. (For interpretation of the references to colour in this figure legend, the reader is referred to the web version of this article.)

3.3. False and missing branches

A qualitative example illustrating the difference among three skeletonization methods at various noise levels has been shown in Fig. 6. The new method successfully stopped noisy branches at all

Table 1

Average false branches by three curve skeletonization methods on five airway phantoms at different levels of noise. None of the three algorithms missed any airway branches up to the 5th anatomic generation of tree.

Noise	Lee et al.	Palágyi et al.	Our method
None	0.8	0	0
Low	4.4	3.8	0
Medium	9.2	9.8	0
High	12.8	14.6	0

noisy granulates on the airway boundary. Although the algorithm by Palágyi et al. did not produce any false branch for no noise phantoms, it failed to do so for noisy phantoms. The algorithm by Lee et al. produced false branches even for no noise phantoms.

A quantitative experiment was carried out by two mutually-blinded experts examine the performance of different algorithms in terms of false and missing branches. Each expert independently labelled the false and missing branches in each airway skeleton by visually comparing it with the matching volume tree. The results of this experiment for airway phantoms at different noise levels are summarized in Table 1. It is worth noting that the quantitative results of

Table 2

Comparison of false branch performance on ten original CT-derived human airway trees without down-sampling or addition of external noise.

#False branch	Lee et al.	Palágyi et al.	Our method
Average	6.5	6.9	0.5
Std. dev.	4.4	4.1	1.1
Maximum	14	15	3

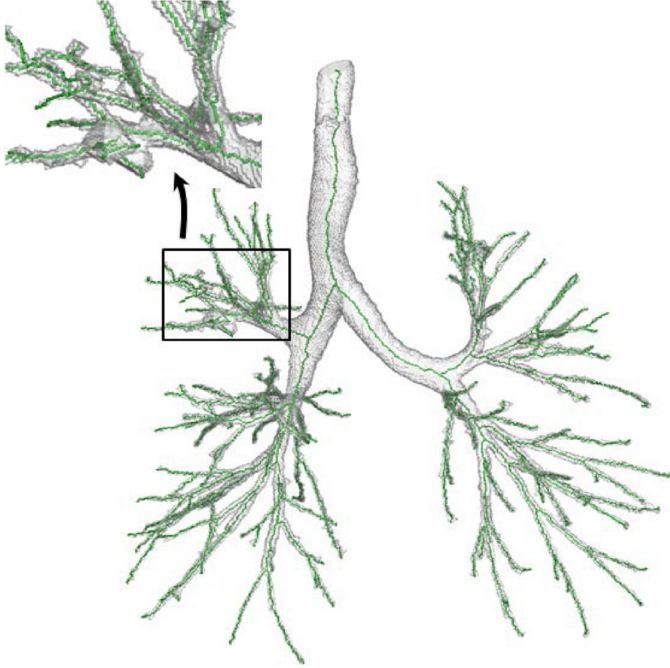


Fig. 8. Illustration of the airway tree where the new method generated three false branches. In this case, a large segmentation leakage occurs on the airway peripheral branch, which causes the generation of three false branches by the new algorithm.

Table 1 is consistent with the observation of Fig. 6. The performance of the new method in terms of false skeletal branches is always superior to the other two methods and the difference is further exacerbated at higher noise levels.

Besides the airway phantoms, ten original segmented human airway trees without down-sampling or addition of external noise were used and analyzed. The labelling of false and missing branches for these original airway trees was confined up to the fifth generation of airway branches because the confidence of labelling a false or missing branch beyond the fifth generation was low due to limited resolution even by the experts. The results are summarized in Table 2. Altogether, the new method generated five false branches among which three false branches were generated in one data set. After a careful look of the specific image data, a segmentation leakage was found at a peripheral airway branch in the right upper lobe and three false branches were generated around that leakage; see Fig. 8. On the other hand, the other two methods generated 65 and 69 false branches. Thus, both qualitative illustrations as well as results from quantitative experiments demonstrate the superiority of the new method in stopping false branches while missing no true branch.

3.4. Efficiency

Computational efficiency of our method was compared with Lee et al., Palágyi et al., and Bitter et al.'s methods. For this experiment, ten original CT-derived human airway tree (average image size: $368 \times 236 \times 495$ voxels) without down-sampling, smoothing, or external noise were used. First, let us examine the relation between the computation complexity of our method and different tree-properties as discussed

Table 3

Average computation time by different algorithms on 10 human airway trees (average image size: $368 \times 236 \times 495$).

Lee et al.	Bitter et al.	Palágyi et al.	Our method
15.4 min	21.1 min	6 s	82 s

in Section 2.5. The average number of terminal branches observed in the ten airway trees used for this experiment was 121.7 and the average number of iterations required by our algorithm was 7.1, which is close to $\log_2 N = \log_2 121.7 = 6.93$ and better than the observed average tree-depth of 11.6 which is close to $\sqrt{N} = \sqrt{121.7} = 11.03$.

The observed average computation time by different methods for these 10 airway trees are reported in Table 3. All the algorithms are implemented in C++ and have run on a PC with a 2.0 GHz Intel CPU. Although, our algorithm is slower than Palágyi et al.'s algorithm [41], the computation time is comparable on the order of seconds, and it is significantly faster than the other two methods. Especially, the improvement in computational complexity as compared to Bitter et al.'s algorithm, which falls under the same category of the new method, is encouraging. This improvement is primarily contributed by enabling multiple skeletal branch detection in one iteration as introduced in this paper.

4. Conclusion

A new algorithm of computing curve skeleton based on minimum cost path for three-dimensional tree-like objects has been presented and its performance has been thoroughly evaluated. The new method uses an initial root seed voxel to grow the skeleton, which may be computed using an automated algorithm. A novel path-cost function has been designed using a measure of local significance factor, which forces new branches to adhere to the centerline of an object. The method uses global contextual information while adding a new branch, which contributes additional power to stop false or noisy branches. Quantitative evaluative experiments on realistic phantoms with known centerlines have demonstrated that the new method is more accurate than conventional existing methods. The other experiment using airway tree data has shown that the new method significantly reduces the number of noisy or false branches as compared to two conventional methods. The new method also reduced the order of computational complexity from the number of terminal branches in a tree to the worst case performance of tree-depth. Experimental results demonstrated that, on an average, the computation complexity is reduced to $O(\log N)$, where N is the number of terminal tree branches.

Acknowledgments

The authors would like to thank Prof. Palágyi for kindly providing the source code of their thinning algorithm used in our comparative study. Also, the authors would like to thank Ms. Feiran Jiao for helping with statistical analysis, and Prof. Xiaodong Wu and Mr. Junjie Bai for providing with references related to computational analysis. This work was supported by the NIH grant R01 HL12986.

References

- [1] C. Arcelli, G. Sanniti di Baja, A width-independent fast thinning algorithm, *IEEE Trans. Pattern Anal. Mach. Intell.* 7 (1985) 463–474.
- [2] C. Arcelli, G. Sanniti di Baja, L. Serino, Distance-driven skeletonization in voxel images, *IEEE Trans. Pattern Anal. Mach. Intell.* 33 (2011) 709–720.
- [3] D. Attali, G. Sanniti di Baja, E. Thiel, Skeleton simplification through non significant branch removal, *Image Process. Commun.* 3 (1997) 63–72.
- [4] I. Bitter, A.E. Kaufman, M. Sato, Penalized-distance volumetric skeleton algorithm, *IEEE Trans. Visual. Comput. Graph.* 7 (2001) 195–206.
- [5] H. Blum, A transformation for extracting new descriptors of shape, *Models Percept. Speech Vis. Form* 19 (1967) 362–380.

- [6] H. Blum, R. Nagel, Shape description using weighted symmetric axis features, *Pattern Recognit.* 10 (1978) 167–180.
- [7] G. Borgefors, Distance transform in arbitrary dimensions, *Comput. Vis. Graph. Image Process.* 27 (1984) 321–345.
- [8] G. Borgefors, Distance transformations in digital images, *Comput. Vis. Graph. Image Process.* 34 (1986) 344–371.
- [9] G. Borgefors, I. Nyström, G. Sanniti di Baja, Computing skeletons in three dimensions, *Pattern Recognit.* 32 (1999) 1225–1236.
- [10] A. Brennecke, T. Isenberg, 3D shape matching using skeleton graphs, *SimVis. Cite-seer* (2004) 299–310.
- [11] C. Chen, D. Jin, Y. Liu, F.W. Wehrli, G. Chang, P.J. Snyder, R.R. Regatte, P.K. Saha, Volumetric topological analysis on in vivo trabecular bone magnetic resonance imaging, in: G. Bebis, et al. (Eds.), *International Symposium on Visual Computing (ISVC)*, Springer, Las Vegas, NV, 2014, pp. 501–510.
- [12] S.Y. Chen, J.D. Carroll, J.C. Messenger, Quantitative analysis of reconstructed 3-D coronary arterial tree and intracoronary devices, *IEEE Trans. Med. Imaging* 21 (2002) 724–740.
- [13] L.D. Cohen, Multiple contour finding and perceptual grouping using minimal paths, *J. Math. Imaging Vis.* 14 (2001) 225–236.
- [14] L.D. Cohen, T. Deschamps, Segmentation of 3D tubular objects with adaptive front propagation and minimal tree extraction for 3D medical imaging, *Comput. Meth. Biomech. Biomed. Eng.* 10 (2007) 289–305.
- [15] L.D. Cohen, R. Kimmel, Global minimum for active contour models: A minimal path approach, *Int. J. Comput. Vis.* 24 (1997) 57–78.
- [16] N.D. Cornea, D. Silver, P. Min, Curve-skeleton properties, applications, and algorithms, *Vis Comput. Graph. IEEE Trans.* 13 (2007) 530–548.
- [17] L. da Fontoura Costa, R.M. Cesar Jr, *Shape Analysis and Classification: Theory and Practice*, CRC press, 2000.
- [18] T. Deschamps, L.D. Cohen, Fast extraction of minimal paths in 3D images and applications to virtual endoscopy, *Med. Image Anal.* 5 (2001) 281–299.
- [19] P. Flajolet, A. Odlyzko, The average height of binary trees and other simple trees, *J. Comput. Syst. Sci.* 25 (1982) 171–213.
- [20] P.J. Giblin, B.B. Kimia, A formal classification of 3D medial axis points and their local geometry, *IEEE Trans. Pattern Anal. Mach. Intell.* 26 (2004) 238–251.
- [21] H. Greenspan, M. Laifenfeld, S. Einar, O. Barnea, Evaluation of center-line extraction algorithms in quantitative coronary angiography, *IEEE Trans. Med. Imaging* 20 (2001) 928–941.
- [22] M.S. Hassouna, A. Farag, S.G. Hushek, 3D Path Planning for Virtual Endoscopy, *International Congress Series*, Elsevier, 2005, pp. 115–120.
- [23] M.S. Hassouna, A.A. Farag, Variational curve skeletons using gradient vector flow, *IEEE Trans. Pattern Anal. Mach. Intell.* 31 (2009) 2257–2274.
- [24] T. He, L. Hong, D. Chen, Z. Liang, Reliable path for virtual endoscopy: ensuring complete examination of human organs, *IEEE Trans. Vis. Comput. Graph.* 7 (2001) 333–342.
- [25] D. Jin, K.S. Iyer, E.A. Hoffman, P.K. Saha, Automated assessment of pulmonary arterial morphology in multi-row detector CT imaging using correspondence with anatomic airway branches, in: G. Bebis, et al. (Eds.), *International Symposium on Visual Computing (ISVC)*, Springer, Las Vegas, NV, 2014, pp. 521–530.
- [26] D. Jin, K.S. Iyer, E.A. Hoffman, P.K. Saha, A new approach of arc skeletonization for tree-like objects using minimum cost path, in: *22nd International Conference on Pattern Recognition*, Stockholm, Sweden, 2014, pp. 942–947.
- [27] D. Jin, P.K. Saha, A new fuzzy skeletonization algorithm and its applications to medical imaging, in: *17th International Conference on Image Analysis and Processing (ICIAP)*, Naples, Italy, 2013, pp. 662–671.
- [28] B.B. Kimia, A. Tannenbaum, S.W. Zucker, Shape, shocks, and deformations. I. The components of two-dimensional shape and the reaction-diffusion space, *Int. J. Comput. Vis.* 15 (1995) 189–224.
- [29] R. Kimmel, D. Shaked, N. Kiryati, Skeletonization via distance maps and level sets, *Comput. Vis. Image Process.* 62 (1995) 382–391.
- [30] A.P. Kiraly, J.P. Helferty, E.A. Hoffman, G. McLennan, W.E. Higgins, Three-dimensional path planning for virtual bronchoscopy, *IEEE Trans. Med. Imaging* 23 (2004) 1365–1379.
- [31] L. Lam, S.-W. Lee, C.Y. Suen, Thinning methodologies – a comprehensive survey, *IEEE Trans. Pattern Anal. Mach. Intell.* 14 (1992) 869–885.
- [32] T.-C. Lee, R.L. Kashyap, C.-N. Chu, Building skeleton models via 3-D medial surface/axis thinning algorithm, *CVGIP: Graph. Models Image Process.* 56 (1994) 462–478.
- [33] F. Leymarie, M.D. Levine, Simulating the grassfire transform using an active contour model, *IEEE Trans. Pattern Anal. Mach. Intell.* 14 (1992) 56–75.
- [34] H. Li, A. Yezzi, Vessels as 4-D curves: global minimal 4-D paths to extract 3-D tubular surfaces and centerlines, *IEEE Trans. Med. Imaging* 26 (2007) 1213–1223.
- [35] Y. Liu, D. Jin, C. Li, K.F. Janz, T.L. Burns, J.C. Torner, S.M. Levy, P.K. Saha, A robust algorithm for thickness computation at low resolution and its application to in vivo trabecular bone CT imaging, *IEEE Trans. Biomed Eng.* 61 (2014) 2057–2069.
- [36] K. Mori, J. Hasegawa, Y. Suenaga, J. Toriwaki, Automated anatomical labeling of the bronchial branch and its application to the virtual bronchoscopy system, *IEEE Trans. Med. Imaging* 19 (2000) 103–114.
- [37] G. Németh, P. Kardos, K. Palágyi, Thinning combined with iteration-by-iteration smoothing for 3D binary images, *Graph. Models* 73 (2011) 335–345.
- [38] R.L. Ogniewicz, O. Kübler, Hierarchic voronoi skeletons, *Pattern Recognit.* 28 (1995) 343–359.
- [39] K. Palágyi, A. Kuba, A 3D 6-subiteration thinning algorithm for extracting medial lines, *Pattern Recognit. Lett.* 19 (1998) 613–627.
- [40] K. Palágyi, A. Kuba, A parallel 3D 12-subiteration thinning algorithm, *Graph. Models and Image Process.* 61 (1999) 199–221.
- [41] K. Palágyi, J. Tschirren, E.A. Hoffman, M. Sonka, Quantitative analysis of pulmonary airway tree structures, *Comput. Biol. Med.* 36 (2006) 974–996.
- [42] G. Peyré, M. Péchaud, R. Keriven, L.D. Cohen, Geodesic methods in computer vision and graphics, *Found. Trends Comput. Graph. Vis.* 5 (2010) 197–397.
- [43] C. Pudney, Distance-ordered homotopic thinning: a skeletonization algorithm for 3D digital images, *Comput. Vis. Image Understand* 72 (1998) 404–413.
- [44] P.K. Saha, B.B. Chaudhuri, Detection of 3-D simple points for topology preserving transformations with application to thinning, *IEEE Trans. Pattern Anal. Mach. Intell.* 16 (1994) 1028–1032.
- [45] P.K. Saha, B.B. Chaudhuri, 3D digital topology under binary transformation with applications, *Comput. Vis. Image Understand* 63 (1996) 418–429.
- [46] P.K. Saha, B.B. Chaudhuri, B. Chanda, D.D. Majumder, Topology preservation in 3D digital space, *Pattern Recognit.* 27 (1994) 295–300.
- [47] P.K. Saha, B.B. Chaudhuri, D.D. Majumder, A new shape preserving parallel thinning algorithm for 3D digital images, *Pattern Recognit.* 30 (1997) 1939–1955.
- [48] P.K. Saha, G. Sanniti di Baja, G. Borgefors, A survey on skeletonization algorithms and their applications, *Pattern Recognit. Lett.*, in press.
- [49] P.K. Saha, J.K. Udupa, D. Odhner, Scale-based fuzzy connected image segmentation: theory, algorithms, and validation, *Comput. Vis. Image Understand.* 77 (2000) 145–174.
- [50] P.K. Saha, F.W. Wehrli, Fuzzy distance transform in general digital grids and its applications, in: *7th Joint Conference on Information Sciences*, Research Triangular Park, NC, 2003, pp. 201–213.
- [51] P.K. Saha, F.W. Wehrli, Measurement of trabecular bone thickness in the limited resolution regime of in vivo MRI by fuzzy distance transform, *IEEE Trans. Med. Imaging* 23 (2004) 53–62.
- [52] P.K. Saha, F.W. Wehrli, B.R. Gomberg, Fuzzy distance transform: theory, algorithms, and applications, *Comput. Vis. Image Understand.* 86 (2002) 171–190.
- [53] P.K. Saha, Y. Xu, H. Duan, A. Heiner, G. Liang, Volumetric topological analysis: a novel approach for trabecular bone classification on the continuum between plates and rods, *IEEE Trans. Med. Imaging* 29 (2010) 1821–1838.
- [54] G. Sanniti di Baja, Well-shaped, stable, and reversible skeletons from the (3,4)-distance transform, *J. Vis. Commun. Image Represent.* 5 (1994) 107–115.
- [55] M. Schaap, C.T. Metz, T. van Walsum, A.G. van der Giessen, A.C. Weustink, N.R. Mollet, C. Bauer, H. Bogunovic, C. Castro, X. Deng, E. Dikici, T. O'Donnell, M. Frenay, O. Friman, M. Hernandez Hoyos, P.H. Kitslaar, K. Krissian, C. Kuhnel, M.A. Luengo-Oroz, M. Orkisz, O. Smedby, M. Styner, A. Szymczak, H. Tek, C. Wang, S.K. Warfield, S. Zambal, Y. Zhang, G.P. Krestin, W.J. Niessen, Standardized evaluation methodology and reference database for evaluating coronary artery centerline extraction algorithms, *Med. Image Anal.* 13 (2009) 701–714.
- [56] L. Serino, C. Arcelli, G. Sanniti di Baja, On the computation of the $<3,4,5>$ curve skeleton of 3D objects, *Pattern Recognit. Lett.* 32 (2010) 1406–1414.
- [57] L. Serino, C. Arcelli, G. Sanniti di Baja, Decomposing 3D objects in simple parts characterized by rectilinear spines, *Int. J. Pattern Recognit. Artif. Intell.* 28 (2014).
- [58] K. Siddiqi, S. Bouix, A. Tannenbaum, S.W. Zucker, Hamilton-Jacobi skeletons, *Int. J. Comput. Vis.* 48 (2002) 215–231.
- [59] K. Siddiqi, S.M. Pizer, *Medial Representations: Mathematics, Algorithms and Applications*, Springer, 2008.
- [60] H. Soltanian-Zadeh, A. Shahrokni, M.-M. Khalighi, Z.G. Zhang, R.A. Zoroofi, M. Madah, M. Chopp, 3-D quantification and visualization of vascular structures from confocal microscopic images using skeletonization and voxel-coding, *Comput. Biol. Med.* 35 (2005) 791–813.
- [61] M. Sonka, M.D. Winniford, S.M. Collins, Robust simultaneous detection of coronary borders in complex images, *IEEE Trans. Med. Imaging* 14 (1995) 151–161.
- [62] M. Sonka, M.D. Winniford, X. Zhang, S.M. Collins, Lumen centerline detection in complex coronary angiograms, *IEEE Trans. Biomed. Eng.* 41 (1994) 520–528.
- [63] E. Sorantin, C. Halmaj, B. Erdohelyi, K. Palágyi, L.G. Nyul, K. Olle, B. Geiger, F. Lindbichler, G. Friedrich, K. Kiesler, Spiral-CT-based assessment of tracheal stenoses using 3-D-skeletonization, *IEEE Trans. Med. Imaging* 21 (2002) 263–273.
- [64] J. Staal, M.D. Abramoff, M. Niemeijer, M.A. Viergever, B. van Ginneken, Ridge-based vessel segmentation in color images of the retina, *IEEE Trans. Med. Imaging* 23 (2004) 501–509.
- [65] S. Svensson, Aspects on the reverse fuzzy distance transform, *Pattern Recognit. Lett.* 29 (2008) 888–896.
- [66] Y.F. Tsao, K.S. Fu, A parallel thinning algorithm for 3D pictures, *Comput. Graph. Image Process.* 17 (1981) 315–331.
- [67] J. Tschirren, G. McLennan, K. Palágyi, E.A. Hoffman, M. Sonka, Matching and anatomical labeling of human airway tree, *IEEE Trans. Med. Imaging* 24 (2005) 1540–1547.
- [68] L. Wade, R.E. Parent, Automated generation of control skeletons for use in animation, *Vis. Comput.* 18 (2002) 97–110.
- [69] M. Wan, Z. Liang, Q. Ke, L. Hong, I. Bitter, A. Kaufman, Automatic centerline extraction for virtual colonoscopy, *IEEE Trans. Med. Imaging* 21 (2002) 1450–1460.
- [70] O. Wink, A.F. Frangi, B. Verdonck, M.A. Viergever, W.J. Niessen, 3D MRA coronary artery determination using a minimum cost path approach, *Magn. Reson. Med.* 47 (2002) 1169–1175.
- [71] O. Wink, W.J. Niessen, M.A. Viergever, Multiscale vessel tracking, *IEEE Trans. Med. Imaging* 23 (2004) 130–133.
- [72] W.C. Wong, A.C. Chung, Probabilistic vessel axis tracing and its application to vessel segmentation with stream surfaces and minimum cost paths, *Med. Image Anal.* 11 (2007) 567–587.
- [73] Y. Xu, G. Liang, G. Hu, Y. Yang, J. Geng, P.K. Saha, Quantification of coronary arterial stenoses in CTA using fuzzy distance transform, *Comput. Med. Imaging Graph.* 36 (2012) 11–24.